GEOCHEMISTRY

Felsic volcanism as a factor driving the end-Permian mass extinction

Hua Zhang[1], Feifei Zhang[2], Jiu-bin Chen[3], Douglas H. Erwin[4,5], Drew D. Syverson[6], Pei Ni[2], Michael Rampino[7], Zhe Chi[2], Yao-feng Cai[1], Lei Xiang[1], Wei-qiang Li[2], Sheng-Ao Liu[8], Ru-cheng Wang[2], Xiang-dong Wang[2], Zhuo Feng[9], Hou-min Li[10], Ting Zhang[3], Hong-ming Cai[3], Wang Zheng[3], Ying Cui[11], Xiang-kun Zhu[12], Zeng-qian Hou[10], Fu-yuan Wu[12], Yi-gang Xu[13], Noah Planavsky[6], Shu-zhong Shen[2,13,14]*

The Siberian Traps large igneous province (STLIP) is commonly invoked as the primary driver of global environmental changes that triggered the end-Permian mass extinction (EPME). Here, we explore the contributions of coeval felsic volcanism to end-Permian environmental changes. We report evidence of extreme Cu enrichment in the EPME interval in South China. The enrichment is associated with an increase in the light Cu isotope, melt inclusions rich in copper and sulfides, and Hg concentration spikes. The Cu and Hg elemental and isotopic signatures can be linked to S-rich vapor produced by felsic volcanism. We use these previously unknown geochemical data to estimate volcanic SO_2 injections and argue that this volcanism would have produced several degrees of rapid cooling before or coincident with the more protracted global warming. Large-scale eruptions near the South China block synchronous with the EPME strengthen the case that the STLIP may not have been the sole trigger.

INTRODUCTION

The end-Permian mass extinction (EPME) was the most severe extinction event in the past 500 million years (1), with estimated losses of >81% of marine (2) and >89% of terrestrial species (3). Robust evidence, supported by high-precision U-Pb dating, suggests that the EPME was triggered by the $>4 \times 10^6$ km^3 volcanic eruption of the Siberian Traps large igneous province (STLIP) (4, 5). It has been proposed that the STLIP eruptions released a massive amount of greenhouse and poisonous gases (e.g., CO_2 and SO_2), leading to rapid warming (6, 7), perturbing global carbon, and sulfur cycles (8), potentially causing acid rain deposition, and ultimately expanded anoxic/euxinic zones in the oceans [e.g., (9)]. In this scenario, a combination of these factors led to the loss of land plants and the widespread extinction of tetrapods (3, 10). The links among the global carbon cycle, climate change, and mass extinction are recorded in the global scale 5 to 8 per mil (‰) negative shift in both $\delta^{13}C_{carb}$ and $\delta^{13}C_{org}$ through the mass-extinction interval (5, 8).

Although the STLIP scenario has been widely accepted (4), temporal links between the mass extinction and volcanism were largely based on sedimentary records from South China, specifically, high-resolution isotope dilution thermal mass spectrometry (ID-TIMS) U-Pb dates from two volcanic ash beds (beds 25 and 28) at the Meishan section (5). The Permian-Triassic boundary (PTB) interval is also associated with Hg and Hg isotope anomalies likely linked to volcanic eruptions (11–13), and these anomalies have been used to argue for a causal link between the EPME and STLIP [e.g., (13, 14)]. The Siberian region does not contain direct fossil data nor sedimentary geochemical profiles correlative with other PTB sections. Nonetheless, the correlation in timing and the magnitude of STLIP has led many to interpret it as the primary cause of the EPME (8, 13, 14). Geochronological studies suggest the STLIP started ~300 thousand years (ka) before the EPME interval and persisted for 500 ka after the extinction (4), with the main extinction occurring within an interval of 61 ± 48 ka or less (5, 15). By contrast, in the STLIP region, recent studies showed an earlier prolonged biodiversity decline pattern or no distinct extinction before the STLIP (16). In addition, more than one-third of the erupted volcanic rocks and the entire STLIP intrusive magmatism postdated the EPME horizon (4, 16). These constraints reduce the volume of CO_2 that could plausibly have been injected into the atmosphere ocean system during the EPME (17). These uncertainties have led to suggestions that outgassing from the STLIP alone may have been insufficient to trigger the global climate and environmental changes associated with the EPME event [e.g., (16)].

Here, we document evidence for extensive felsic volcanic activity coincident with the mass extinction—foremost from anomalous copper (Cu) enrichment and large negative Cu isotope ($\delta^{65}Cu$) shifts at four widely dispersed terrestrial PTB sections in southwest China. Our data include terrestrial extinction patterns, organic carbon isotopes, Cu and mercury (Hg) concentrations and isotopes, widespread distribution of coeval volcanogenic materials, and geochemical analyses of melt inclusions in volcanogenic materials from the

[1]LPS, Nanjing Institute of Geology and Palaeontology and Center for Excellence in Life and Paleoenvironment, Chinese Academy of Sciences, Nanjing 210008, China. [2]State Key Laboratory for Mineral Deposits Research, School of Earth Sciences and Engineering and Environment and Frontiers Science Center for Critical Earth Material Cycling, Nanjing University, Nanjing 210023, China. [3]Institute of Surface-Earth System Science, Tianjin University, 92 Weijin Road, Tianjin 300072, China. [4]Department of Paleobiology, MRC-121 National Museum of Natural History, P.O. Box 37012, Washington, DC 20013-7012, USA. [5]Santa Fe Institute, 1399 Hyde Park Road, Santa Fe, NM 87501, USA. [6]Department of Earth and Planetary Sciences, Yale University, New Haven, CT 06511, USA. [7]Departments of Biology and Environmental Studies, New York University, New York, NY 10003, USA. [8]State Key Laboratory of Geological Processes and Mineral Resources, China University of Geosciences, Beijing 100083, China. [9]Institute of Deep Time Terrestrial Ecology and Institute of Palaeontology, Yunnan University, Kunming 650500, China. [10]Institute of Geology, Chinese Academy of Geological Sciences, Beijing 100037, China. [11]Department of Earth and Environmental Studies, Montclair State University, Montclair, NJ 07043, USA. [12]State Key Laboratory of Lithospheric Evolution, Institute of Geology and Geophysics, Chinese Academy of Sciences, Beijing 100029, China. [13]State Key Laboratory of Isotope Geochemistry and Center of Excellence in Deep Earth Science, Guangzhou Institute of Geochemistry, Chinese Academy of Sciences, Guangzhou 510640, China. [14]Key Laboratory of Continental Collision and Plateau Uplift, Institute of Tibetan Plateau Research and Center for Excellence in Tibetan Plateau Earth Sciences, Chinese Academy of Sciences, Beijing 100101, China.
*Corresponding author. Email: szshen@nju.edu.cn

EPME interval. This evidence is best interpreted as the result of vast explosive felsic "super-eruptions" (*18*) from a continental volcanic arc associated with the opening of the Neotethys or closure of the Paleotethys (*19*). Translating these data into estimates of SO_2 injection and temperature changes, we suggest that felsic volcanism in South China was a key contributor to the environmental deterioration that led to the EPME.

Geological background

During the Permian-Triassic transition, the South China block was situated in the tropical eastern Paleotethys and accumulated the most complete PTB record. Most previous PTB studies have focused on marine sedimentary records with relatively few studies of the terrestrial EPME (*5*). The geochronologic, geochemical, and paleoclimate proxy data presented here, along with extinction patterns and marked changes in terrestrial depositional systems and widespread volcanogenic materials, establish links between volcanism and the EPME on land. The four terrestrial PTB sections discussed here are the Guanbachong (GBC), Lubei (LB), and Taoshujing (TSJ) sections in Yunnan and the Longmendong (LMD) section in Sichuan, South China (fig. S1). The relevant strata in these sections are the Lopingian Xuanwei formation, the Permian-Triassic transitional Kayitou formation, and the Lower Triassic Dongchuan formation. They were deposited in swamp and shallow lacustrine environments, and a calm, ever-flooded aqueous environment to semiarid alluvial floodplains with braided river systems, respectively (fig. S2) (*20*, *21*).

The terrestrial EPME in South China

The EPME horizon in the studied sections is defined by the disappearance of the palaeotropical rainforest-type *Gigantopteris* flora in the upper Kayitou formation (i.e., coincident with the Cu and Hg enrichment intervals in the volcanogenic materials discussed below; Figs. 1 and 2). The rainforest-type *Gigantopteris* flora is highly diverse and abundant in the Lopingian (Late Permian) coal-bearing Xuanwei formation and the lower part of the Permian-Triassic transitional Kayitou formation (*20*, *21*). In the middle part of the Kayitou formation, tiny plant fragments (e.g., *Germaropteris* and *Tomiostrobus sinensis*) and Permian-Triassic transitional conchostracans began to dominate the community, but typical Permian plant species persisted. The Cu-enrichment and Hg anomalies occur at an interval between 0.8 and 6.65 m thick in the volcanogenic sandstone immediately above the mass disappearances of the species of *Gigantopteris* flora. In the Cu-enriched interval, charcoal is abundant (*20–22*), and the homogenized cell walls in charcoal fragments suggest that they were products of the ignition of living plants (Fig. 1, D and E, and fig. S3). Although these charcoalified remains are not identifiable to genus or species, they indicate widespread wildfires in Permian tropical forests. Organic carbon isotopic analyses of both bulk rocks and charcoals show that the $\delta^{13}C_{org}$ values in the Kayitou formation are notably more negative than those in the Xuanwei formation, with a negative excursion of 4.08‰ immediately above a volcanic ash bed at the last coal bed. Reflectance values of charcoal are high below the ash bed but become much lower in the overlying Kayitou formation, indicating the paleo-wildfire types have changed from crown fires to surface fires as rainforests declined during the extinction (*22*). Therefore, the interval from the last horizon containing abundant plant fossils to the last charcoal-rich level constrains the EPME interval in the terrestrial ecosystem in southwest China (*20*, *21*). In the field, this interval can be readily identified by changes in rock color from alternating greenish/brownish to maroon dominated and by the presence of widespread syndepositional sandstone breccia and pedogenic calcite nodules commonly with a fungi spike. Together, these features signify the rapid collapse of soil systems during and after the destruction of the vegetation (figs. S2 and S4). Upsection mudrocks display a purely purple color without plant fragments, which indicates a seasonally dry environment (*20*, *21*).

Fig. 1. Photographs and photomicrographs of the Cu-rich sulfide and charcoal from the terrestrial Permian-Triassic transition. (**A**) Rock sample from TSJ-71a, TSJ section; (**B**) rock sample LB-16 from LB section; (**C**) rock sample from GBC-3b-3, GBC section; (**D**) rock sample of bed TSJ-71a with malachite and charcoal from TSJ section; and (**E**) rock sample of bed LMD-38-2 with malachite from LMD section. Photo credit: H. Zhang, Nanjing Institute of Geology and Palaeontology.
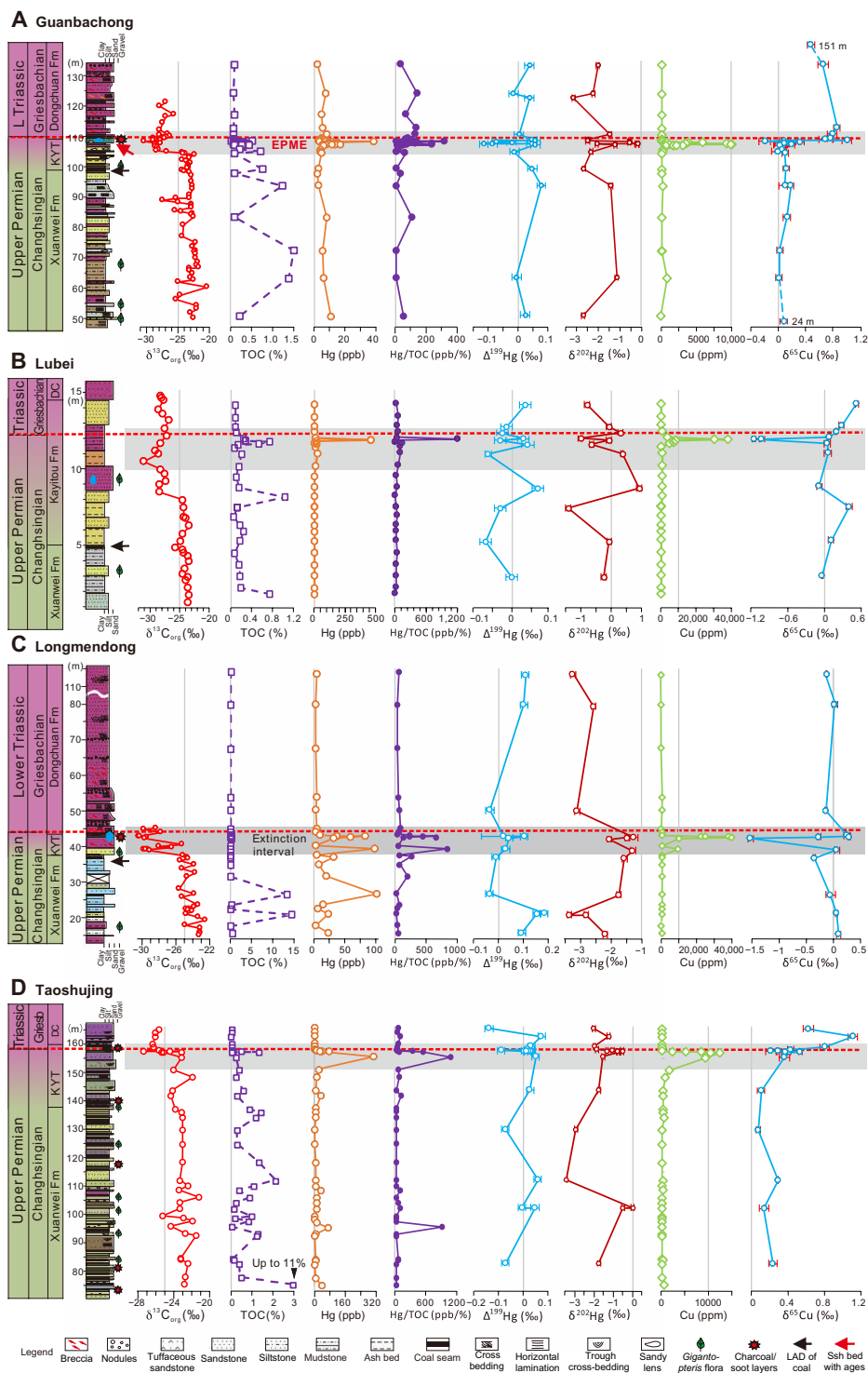
Fig. 2. Organic carbon isotope (δ13Corg), TOC, Hg/TOC, mercury concentration (Hg), mercury MDF (δ202Hg) and MIF (Δ199Hg), copper concentration (Cu), and isotopes (δ65Cu) of study sections. (**A**) GBC section, (**B**) LB section, (**C**) LMD, and (**D**) TSJ section. The red dashed lines indicate the estimated PTB based on (20, 21). Gray bars are the terrestrial EPME intervals. The horizontal bars in the isotope profiles indicate SD (2σ) values, which, in many cases, are smaller than the symbol size. Source data are provided in tables S1 to S4.

The δ13Corg excursions associated with the EPME in the GBC, LMD, and LB sections have been previously reported (20–22). Our δ13Corg data from the TSJ section confirm a 5 to 8‰ δ13Corg shift within the extinction interval (Fig. 2). Similar negative shifts in terrestrial sequences have also been reported from the North China block (23), the Karoo basin (24), eastern Australia (10), and eastern Greenland (25), suggesting that the terrestrial carbon cycle perturbation was a global phenomenon. This δ13Corg negative excursion is

commonly associated with the globally recognized $\delta^{13}C_{carb}$ negative excursion in marine PTB sections (e.g., Meishan and Greenland), which has been widely used for correlation between the terrestrial and the marine EPME (20, 21, 25).

RESULTS

Cu concentrations and Cu sulfide

A total of 128 samples were analyzed for a full suite of major and trace elements from the four terrestrial PTB sections (Appendix A in the Supplementary Materials). Notable Cu enrichments occur at the terrestrial EPME interval at all four sections (Figs. 1 and 2, fig. S4, and table S1). Bulk rock Cu contents increase from a background level of <500 parts per million (ppm) to greater than 10,000 ppm in the EPME interval at all sections and up to 40,044 ppm at the LMD section. In the overlying sandstones of the Lower Triassic Dongchuan formation, the Cu contents dropped below 50 ppm. The copper-rich interval is 1.2 m thick at GBC, ~3.7 m at LMD, 0.8 m at LB, and 6.65 m at TSJ, respectively (table S1). The high Cu concentration is associated with Cu-rich minerals such as malachite and chalcocite. Green oxidized malachite can be seen in the stratigraphic interval (Fig. 1). The malachite minerals are often associated with abundant charcoal, but many form small concretions of droplets on bedding planes (Fig. 1, C and E).

The copper sulfides are predominantly hosted in the volcano-sedimentary sequence at the PTB; no sulfides have been found stratigraphically below or above the boundary. These Cu-rich sulfides are chalcocite group minerals in thin layers or lenses and are coarse grained, anhedral, and homogeneous without replacement by other sulfides. The secondary mineral is malachite, as overgrowths or filling in fractures within the sulfides. In addition to the sulfides in lenses or layers, abundant sulfide inclusions occur in anhedral quartz in the volcanogenic rocks. The quartz crystal fragments containing melt inclusions are euhedral to subhedral, homogeneous, and have sharply angular outlines, which is consistent with a volcanic origin (Fig. 3 and fig. S6G). Mineralogical and chemical studies of melt inclusions in quartz crystal fragments from the sample (TSJ-71a) within the Cu and Hg peaks at the TSJ section (Fig. 1A and fig. S6F) indicate Cu concentration up to 186 ppm and are acidic in composition with SiO_2 contents of 76.5 to 77.2 weight % (wt %) (Fig. 3, C and D, and table S6). They are characterized by an average Cu:S ratio of 1.8 and analyzed by energy-dispersive x-ray spectroscopy after being exposed to the surface (Fig. 3B).

$\delta^{65}Cu$ excursions

A total of 64 samples from the four sections were analyzed for $\delta^{65}Cu$ and showed an overall variation from −1.52 to 1.11‰ (table S3). All four studied sections show distinct $\delta^{65}Cu$ excursions that were contemporaneous with the Cu enrichment across the EPME interval (Fig. 2) (see more detailed description in the Supplementary Materials). Before the extinction horizon, the $\delta^{65}Cu$ values show a relatively small variation around zero in all sections (table S3), consistent with those of igneous rocks, and suggesting that volcanogenic detrital materials from terrestrial weathering were the primary source of sedimentary Cu (Figs. 1 and 2 and tables S3) (26, 27). However, different patterns of $\delta^{65}Cu$ are observed through the extinction horizon in different sections (Fig. 2). At the two sections associated with higher Cu enrichment (~40,000 ppm, LB and LMD sections),

there was a distinct negative excursion of $\delta^{65}Cu$ (to −1.16 and −1.52‰, respectively) immediately below the extinction horizon, followed by a return to the preextinction value (LMD) or a gradual positive shift to 0.53‰ (LB). In contrast, the GBC and TSJ sections, which are associated with relatively lower Cu enrichment (~10,000 ppm), show a slight negative excursion at the extinction horizon, followed by a rapid and strong positive shift (to 0.99 and 1.11‰, respectively) above the extinction interval. The negative excursions in $\delta^{65}Cu$ across the Cu-enriched intervals (i.e., within the EPME horizon) are inconsistent with oxidative surface weathering and metal re-enrichment process as a source of the Cu enrichments, which would produce higher $\delta^{65}Cu$ values in the Cu-enriched intervals [e.g., (26, 27)], implying other large allochthonous input.

Hg concentration and Hg isotopes

Hg elemental and isotopic abundances have been widely used as chemical proxies of global volcanic events, particularly in the EPME (12). The Cu-rich horizon also contains a distinctive Hg enrichment. The peak Hg concentrations are 39 parts per billion (ppb) at GBC, 101 ppb at LMD, 462 ppb at LB, and 300 ppb at TSJ, whereas the background values above and below the extinction interval are one to two orders of magnitude lower (Fig. 2, fig. S4, and table S1, Appendix A in the Supplementary Materials). Since Hg is hosted mainly by organic matter, Hg concentrations were normalized to total organic carbon (TOC) to discern enrichments independent of variations in TOC. Our analyses of TOC from the four sections indicate that TOC in the Lopingian Xuanwei formation is highly variable. The Hg enrichment cannot be interpreted as enhanced scavenging by organic matter because the TOC-normalized Hg (Hg/TOC) shows similar spikes to the Hg concentration. The highest Hg/TOC spikes from the EPME interval in the four sections range from 2 to 1199 μg/kg per wt %, whereas the Hg/TOC ratios above and below the extinction interval are generally lower except for a few individual samples (Fig. 2, fig. S4, and table S1).

We also observed distinct shifts in both mass-dependent fractionation (MDF; represented by $\delta^{202}Hg$) and mass-independent fractionation (MIF; represented by $\Delta^{199}Hg$) of Hg isotopes across the EPME transition but with different patterns in the four sections (Fig. 2; see detailed description in the Supplementary Materials). In both GBC and TSJ sections, $\Delta^{199}Hg$ shows a negative shift from 0.05 to −0.11 and −0.07 to 0.01‰ at the extinction horizon, accompanied by a positive shift of $\delta^{202}Hg$ from −2.05 to −0.15‰ (i.e., the magnitude of the shift is 1.9‰) and from −1.49 to −0.50‰, respectively (Fig. 2 and table S4). In contrast, at the LB section, both $\Delta^{199}Hg$ and $\delta^{202}Hg$ fluctuated around 0.0‰ from the Xuanwei formation to the lowest Triassic, with relatively minor excursions present at the extinction intervals (Fig. 2B). At the LMD section, a positive shift of $\Delta^{199}Hg$ and a minor negative excursion of $\delta^{202}Hg$ are slightly displayed (Fig. 2C and table S4).

DISCUSSION

The primary depositional signature of Cu anomalies

Copper enrichments (compared to the Earth's crust average of 28 ppm) [e.g., (28)] are most commonly associated with secondary mineralization. However, neither hydrothermal systems nor weathered products from the parent materials at other horizons are plausible explanations for the extreme Cu enrichments in our studied terrestrial EPME interval. These Cu enrichments consistently occur in
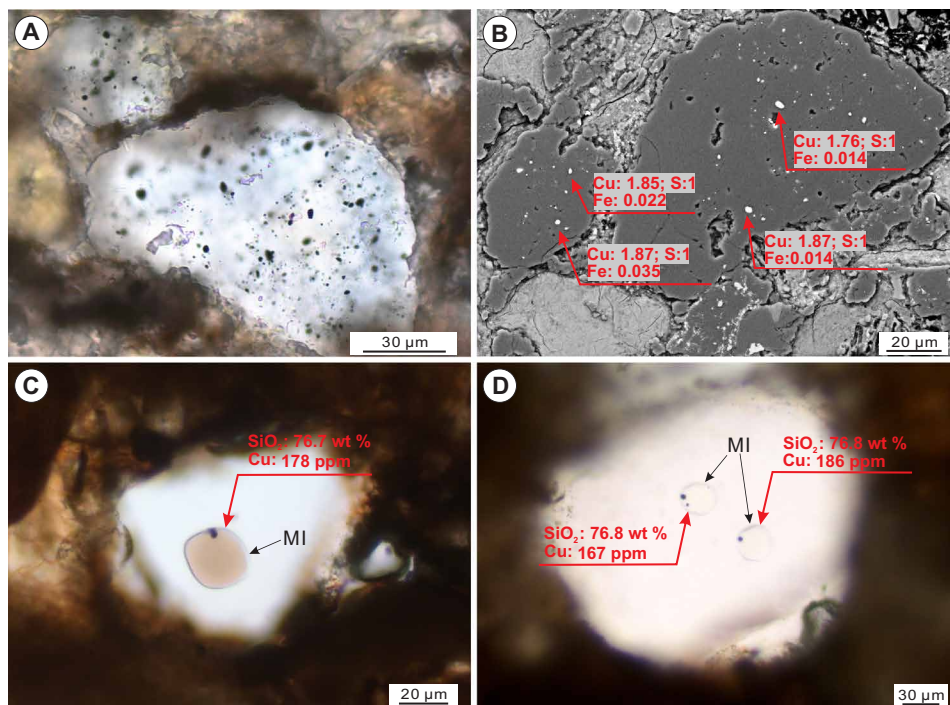
Fig. 3. Photomicrographs of inclusions. (**A** and **B**) Sulfide inclusions in anhedral quartz and (**C** and **D**) melt inclusions in quartz crystal fragments. Sample TSJ-71a from the Cu-enriched horizon of the TSJ section in Fig. 1A. Photo credit: Z. Chi and P. Ni, Nanjing University.

a consistent, narrow stratigraphic interval independent of lithology and extend over geographic distances of >340 km (fig. S1). Although a recent provenance study suggests that the sandstones in the Lopingian Xuanwei formation are partly derived from the underlying Emeishan eruptive materials (*29*), no distinctive Cu and Hg anomalies are found at horizons below or above the EPME interval (Fig. 2 and fig. S4). Cu concentrations are reduced in the sections affected by seawater and usually not detected from normal marine sections, while Hg anomalies are widely found, potentially because copper (II) sulfide has a much higher solubility in seawater than mercury (II) sulfide (*30*).

The sharp negative δ^{65}Cu peaks correspond to much higher Cu enrichments (LB and LMD sections), allowing us to exclude further post-depositional transformation of weathered materials into Cu-rich sulfides under reducing conditions (*26*). The redox transformation of Cu in surface environments would enrich ^{63}Cu (thus lower δ^{65}Cu values) in secondary sulfides (*27*, *31*). Because of the Cu isotope mass balance, the higher enrichment of Cu derived from this redox mobilization process would be associated with a δ^{65}Cu close to that of the initial weathered materials, contrary to our observation that the Cu enrichments are associated with anomalously negative δ^{65}Cu values (Fig. 2) (see more detailed discussion in the Supplementary Materials). However, given the current understanding of Cu isotope systematics, the sharp negative peak in δ^{65}Cu and the simultaneous strong Cu enrichment observed across the EPME in the LB and LMD sections are best explained by the direct input of Cu (I) sulfide emitted from nearby felsic volcanism (Supplementary Materials). Below, we propose and develop the idea that large-scale felsic volcanism around the South China block is the source of the Cu and Hg anomalies, rather than the STLIP.

Cu and Hg anomalies linked to felsic volcanism near the South China block

Several lines of evidence indicate that intensive felsic volcanism near the South China block occurred around the EPME interval. First, volcanic tuffs and pyroclastic sandstone in southern and southwestern parts of South China (*15*, *21*, *32*) and intermediate-acidic volcanic and intrusive rocks have been widely reported at the PTB interval in southern and southwestern China and northern Vietnam (*33*, *34*), the Jinshajiang orogenic belt in southwest Yunnan, and eastern Kunlun mountains in northwestern China (*32*, *35*, *36*). These suggest magmatic arcs within the Paleotethys and Neotethys oceans were distributed widely over 1200 km. Second, high-precision geochronologic studies of those volcanogenic materials are consistent with the EPME in age. Five chemical abrasion (CA)-ID-TIMS dates from the tuff/tuffaceous sandstone at Penglaitan, Guangxi, were dated with the EARTHTIME ^{202}Pb-^{205}Pb-^{233}U-^{235}U tracer solution between 251.991 ± 0.029 and 251.903 ± 0.030 Ma (*15*). A CA-ID-TIMS date from a tuff bed at Heshan, Guangxi, was dated 252.41 ± 0.08 Ma with the MIT-mixed ^{233}U-^{235}U-^{205}Pb tracer solution. Seven zircon grains were analyzed from the tuffaceous sandstone sample with the highest Cu peak at the Guangbachong section (GBC3b) and cluster around 252 to 253 Ma, overlapping with the date of bed 25 at Meishan (*21*). The ages of two ash beds in the EPME interval at the marginal marine Zhongzhai section and one ash bed at the terrestrial Chahe section in Guizhou near the studied sections are consistent with bed 25 at Meishan (*21*). Third, we propose that the Cu concentration and isotope anomalies were most likely derived from the direct deposition of sulfide droplets from magmatic vapor or aerosols in association with large-scale felsic eruptions. Melt inclusions are preserved in quartz crystal fragments that represent the burst splinter of phenocryst in magma

during explosive eruptions. Given the low diffusion coefficient of Cu ($<10^{-17}$ m^2/s) during diagenesis (37), the high Cu concentrations of the melt inclusions suggest that the original magmatic environment was enriched in Cu. The Cu/S ratios and a low Fe content (Fig. 3B) suggest that the sulfides are similar to the sulfide precipitation in vapor-rich inclusions in magmatic phenocrysts and sulfide inclusions in fumarole sublimates. These lines of evidence together suggest that these sulfide droplets were from a magmatic vapor or aerosol (38), and their consistent mineralogical and chemical compositions with the host volcanogenic materials strongly indicate an origin from the nearby felsic volcanism.

Chalcocite group minerals can occur as supergene products near porphyry Cu deposits (~10 km) and were formed by complex processes including leaching, oxidation, and replacement of previous sulfides. Such a supergene genesis for the EPME Cu sulfides is contradicted by the extraordinarily widespread distribution of the chalcocite enrichments ($>90,000$ km^2), their tight restriction to the EPME interval, and the absence of typical replacement textures.

The evidence presented here is also inconsistent with the nearby massive Emeishan basalts as a candidate Cu source. Underlying or adjacent altered basement containing basalt-dominated volcanic rocks is often an important source of Cu for some strata-bound copper deposits (39). Extremely thick red bed and evaporite sequences are essential to provide the oxidized brine to leach and transport soluble cupric compounds from the basalt. However, the geochronologic data and the lack of nearby thick red bed sediments precludes Cu leaching from Emeishan basalts. Moreover, if the Cu had been leached from basement basalts, then enrichment zones should occur at various overlying horizons with reducing facies; no leaching model can account for the restriction of the Cu to a specific time-equivalent stratigraphic interval in a wide area. Therefore, the Cu-rich sulfides

must either be a primary deposit or were formed by in situ leaching from the volcanogenic materials with high Cu concentration in these strata. In addition, the δ^{65}Cu of primary sulfides deposited from magmatic vapor under volatilization typically have low δ^{65}Cu values (Fig. 4). This is because extreme degassing results in highly negative δ^{65}Cu values of the vapor due to the ^{65}Cu depletion from the magma during the initial stages of degassing prior to a massive eruption (Fig. 4) (26, 40). This is consistent with the negative δ^{65}Cu values observed in the LB and LMD sections, suggesting that the highly enriched Cu in these two sections most likely captured more deposition of Cu(I) sulfide droplets from the volcanic plume.

In comparison with the LB and LMD sections, in the GBC and TSJ sections, the Cu-enriched layers exhibit a negative δ^{65}Cu excursion of smaller magnitude. We interpret this pattern to reflect the admixture of other materials with relatively low Cu contents but higher δ^{65}Cu in addition to the input of Cu (I) sulfide from the volcanic plume. This hypothesis is consistent with the much lower Cu enrichment in these two sections compared to the LB and LMD sections (Fig. 2, B and C). These additional materials could be soils or organic materials derived from increased continental weathering (20). Volcanic eruptions caused widespread wildfires (22) and wiped out the end-Permian *Gigantopteris*-bearing rainforest vegetation in South China, resulting in a rapid collapse of the soil system and enhanced weathering (20, 21). The GBC and TSJ sections may have captured the products of the oxidative weathering, which is enriched in ^{65}Cu (Supplementary Materials). Abundant fossil charcoal representing terrestrial vegetation debris (see fig. S3) found in these two sections supports this hypothesis (21, 22).

The associated Hg concentration spikes are consistent with previously published records from both marine and terrestrial sections and confirm the existence of extensive volcanism that coincided with the EPME event; however, all the Hg spikes and Hg isotopes in
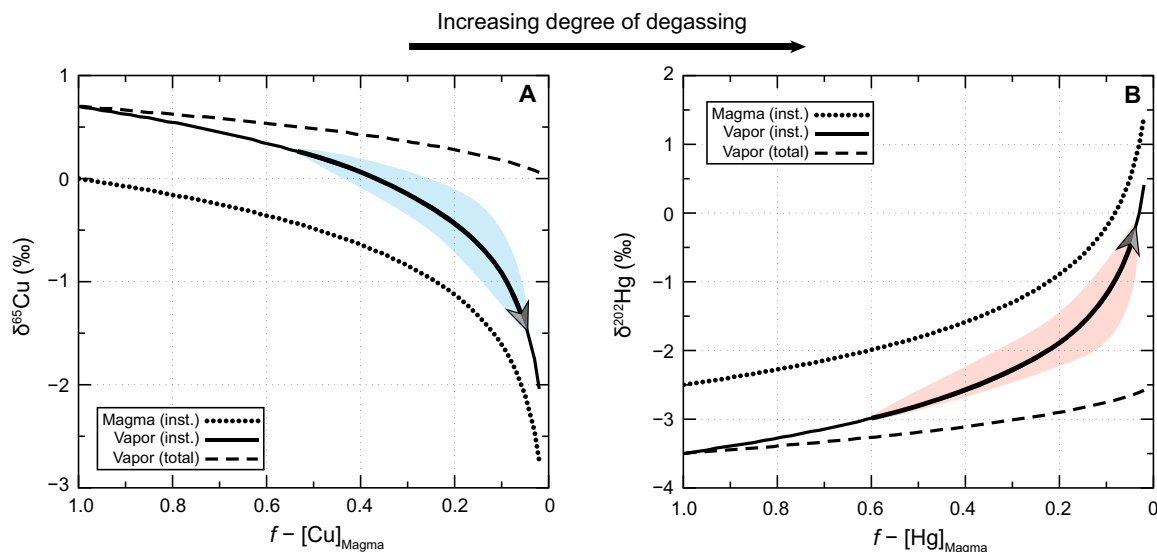

Fig. 4. Rayleigh fractionation model describing the δ^{65}Cu and δ^{202}Hg compositional evolution upon increasing degrees of magmatic degassing of volatilized Cu and Hg. (**A**), Cu; (**B**), Hg. The fraction of Cu and Hg remaining in degassing magma is denoted by $f - [x]_{Magma}$. The magma (inst.), vapor (inst.), and vapor (total) denote the δ^{65}Cu and δ^{202}Hg compositional changes in the residue magma, instantaneous, and cumulative extracted fluids by Rayleigh fractionation; dotted, solid, and dashed lines, respectively. The blue and red shaded areas along the modeled curves represent the range of observed δ^{65}Cu and δ^{202}Hg values upon approaching the PTB, respectively. The large range of decreasing δ^{65}Cu and increasing δ^{202}Hg values in conjunction with massive Cu and Hg enrichments at the terrestrial EPME sections in South China indicate that the metals were sourced from volcanic emissions through substantial degrees of degassing, transport, and deposition of magmatic Cu- and Hg-sulfide minerals.

the EPME interval, including those from South China, have been interpreted as sourced from STLIP (*11*, *12*). The data presented here suggest—or are at least consistent with—a regional source rather than the distant STLIP as the major metal source. In the LB and LMD sections, the Δ^{199}Hg values show little variation across the Hg spike intervals with an average value close to zero (Fig. 2, B and C). These circum-zero odd MIF values are consistent with direct volcanic emission, as shown by measurements of air samples from modern volcanic fumaroles (*41*), and indicate a primary Hg source from local volcanism rather than from more distant volcanic emissions. The reason is that Hg from remote volcanic emission typically shows positive MIF values (*13*) due to photochemical redox reactions of Hg during its atmospheric transport. Therefore, the majority of Hg emitted by STLIP would likely mix with the background atmospheric Hg and participate in the global cycle, which would develop positive MIF before its deposition to land and marine surfaces. In contrast, oxidized Hg [i.e., gaseous Hg(II) and particulate Hg] emitted by local volcanism can deposit in very proximal locations due to their short atmospheric residence time (days to weeks) (*42*) and are thus more likely to retain their original circum-zero MIF. Thus, the lack of notable positive shift of Hg MIF in the LB and LMD sections suggest a dominant input of oxidized Hg species emitted by local volcanism rather than a more distant LIP source.

The relatively lower Hg/TOC ratios (compared to LB and LMD sections) and negative Δ^{199}Hg peaks (Fig. 2) lend further support to a higher continental contribution of Cu in both GBC and TSJ sections (Fig. 5). In these two sections, the negative excursion of Δ^{199}Hg observed in the Cu-enriched layers is consistent with the range of Δ^{199}Hg in terrestrial soil and vegetation (*43*). In general, continental soils and vegetation have slightly negative odd MIF (*43*). Similar

negative excursions of odd MIF across the EPME have been observed in several marine sections globally (*13*) and were interpreted as evidence for enhanced terrestrial weathering and erosion due to the loss of vegetation. As a result, the negative excursion of Δ^{199}Hg in GBC and TSJ sections may indicate accelerated rates of terrestrial weathering due to wildfires and devegetation and collapse of soil systems as evidenced by abundant fossil charcoal (see further discussion in the Supplementary Materials) (*20–22*).

Explosive super-eruptions from South China linked to the EPME event

The Cu- and Hg-rich intervals from the four studied terrestrial sections are correlative with the EPME interval at the Meishan section based on biostratigraphic and geochronologic data, global $\delta^{13}C_{org}$ excursions, and Hg anomalies (*20*, *21*). Data presented here strongly support the source of the massive Cu and Hg enrichments at the terrestrial EPME sections in South China from magmatic vapor erupted from nearby felsic super-eruptions (Fig. 5). We argue that these data and interpretations are inconsistent with degassing and other environmental triggers generated by the STLIP as the sole trigger of the EPME event (*4*, *5*). Rather, because metal enrichment event derived from explosive volcanism correlates precisely with the global negative excursions of $\delta^{13}C_{org}$, which marked the EPME event on land and in the sea (*10*, *20*, *21*, *25*) and based on basic assumptions about the effects of explosive felsic volcanism, this process likely triggered regional or possibly global environmental changes and the EPME. The thickness and number of ash beds and pyroclastic material and distributions of volcanic rocks have been commonly used to estimate source distances (*44*). Although detailed thickness data and high-precision dates of many ash beds around the PTB in South
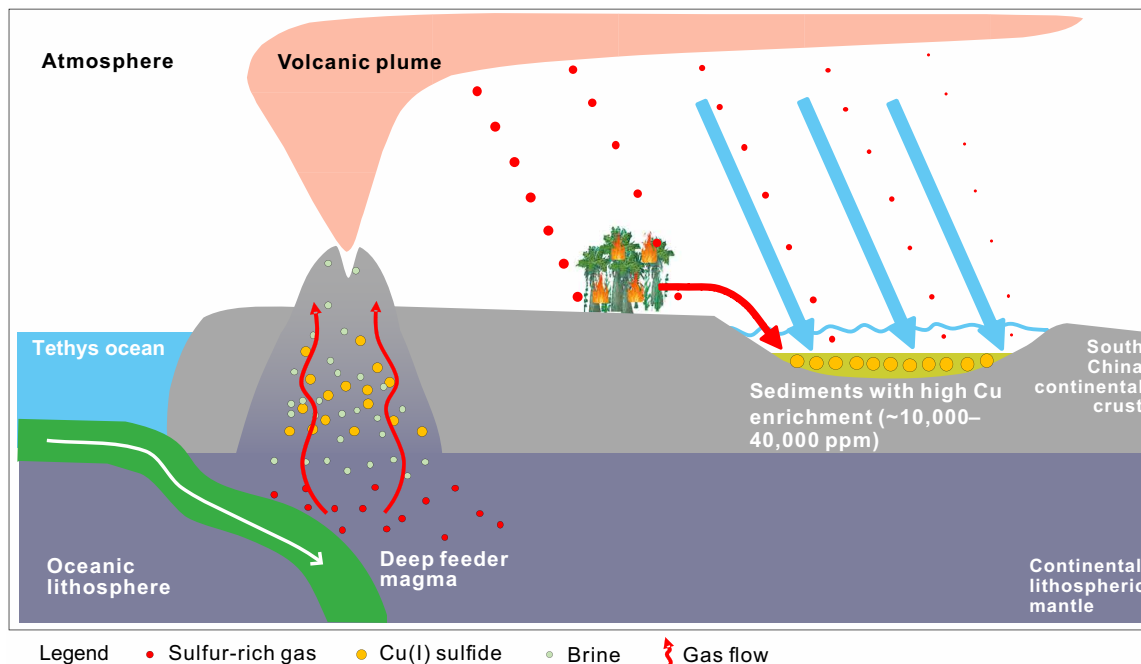

Fig. 5. Schematic showing the formation process of the copper-rich deposits within the EPME interval in South China. The copper-rich deposits during the EPME interval at GBC and TSJ sections showing relatively less input from volcanic aerosol and more from vegetation, soil, and oxidative weathering; whereas the deposits at LB and LMD sections showing more input from volcanic aerosol and relatively less from vegetation, soil, and oxidative weathering.

China are not available, there is a general increase in thickness and number from northern to the southern and southwestern parts of South China. Coarser pyroclastic materials outcrop widely in Guangxi, Guizhou, and Yunnan provinces in South China (fig. S6) (*15*, *21*, *32*) and intermediate-acidic volcanic and intrusive rocks are widely distributed in western Guangxi, Yunnan, and Hainan; northern Vietnam (*33*, *34*); and eastern Kunlun area in northwestern China (fig. S7) (*32*, *35*). Paleogeographic mapping of previously reported volcanogenic felsic materials and Hg anomalies within the EPME interval show them mainly distributed around the Tethyan ocean and the Palaeo-Pacific margin of southern Gondwana (fig. S7), indicating eruptive centers south or/and southwest of the South China block rather than Siberia.

Silicic explosive volcanism as the source responsible for the extreme metal enrichment within the EPME interval in South China rather than STLIP is also consistent with lithological evidence from ash beds in Meishan and other PTB sections in South China. Despite the fact that the causal linkages between Hg spikes across the EPME from other regions and the super-eruptions from South China are uncertain, coeval silicic eruptions have been reported from eastern Australia (*10*, *45*), South America (*46*), southern Africa (*47*), and West Antarctica (*48*) (fig. S7).

We can estimate a minimum total volume of Cu released, assuming that the Cu-rich horizon is about 1.0-m thick (as observed in the field). A conservative estimate (using the documented range of the enrichment) would be >1.9 billion tons of Cu from South China Block volcanism. This is equivalent to the mass of Cu in ~9100 to 18,100 km^3 of magma with 100 or 50 ppm Cu, respectively. Previous studies of large-scale volcanic eruptions (*49*, *50*) indicate the eruption of this volume of magma could emit a few billion tons of SO_2 (Fig. 6) (*50*). Corroborating evidence of a massive release of volcanic SO_2 is provided by the significant Hg enrichment (~47,000 tons) and the large range in negative $\delta^{202}Hg$ isotope values observed within the Cu-rich horizon (Figs. 4 and 6; see the Supplementary Materials). For example, the Hg/SO_2 mass ratios representative of emissions from large-scale explosive volcanic eruptions lie between 10^{-5} and 2×10^{-4} (*51*), from which we estimate 0.24 to 4.71 billion tons of SO_2 would have been emitted; this minimum eruptive flux is ~10 to 200 times than the modern annual volcanic SO_2 flux (*49*, *50*). Model estimates from the Community Earth System Model 1 suggest such a massive SO_2 release would lead to immediate post-eruptive atmospheric cooling of >4°C on a thousand-year time scale [e.g., a brief "volcanic winter"; (*15*, *52*)] before the previously reported rapid global warming across the EPME [also supported by a recent thallium isotope study (*53*)] (*15*). However, multiple factors, such as the extent of sulfur aerosols penetrating the tropopause to the stratosphere, would have affected the actual extent of atmospheric cooling [e.g., (*54*, *55*)]. There is tentative evidence from conodont oxygen isotopes for an estimated 4°C cooling at the EPME at the highly expanded Penglaitan section in Guangxi province (*6*, *7*, *15*), which is close to the minimum Hg- and Cu-based cooling estimates (Fig. 6; see the Supplementary Materials). Furthermore, recent modeling results (*56*) indicate that a warming climate, such as induced through the long-term input of CO_2 into the atmosphere from volcanism, can effectively amplify short-term atmospheric cooling effects through the enhanced delivery into and increased residence time of SO_2 in the stratosphere from massive explosive felsic volcanism events at scales similar to what is predicted from Cu and Hg mass balance data presented in this study (Fig. 6).
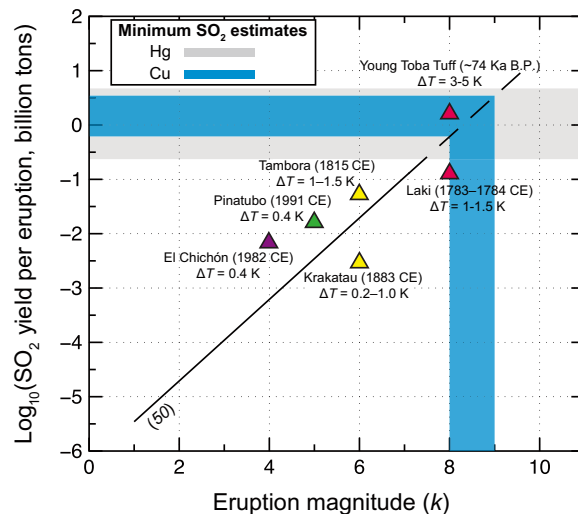

Fig. 6. SO₂ yield per eruption as a function of eruption magnitude, *k*. The estimated SO_2 yield per eruption is determined through Hg mass balance (gray area), constrained by Hg/SO_2 emission estimates for eruptive volcanic events and the mass of Hg in the deposit (*51*). Independently, the estimated SO_2 yield per eruption, determined through Cu mass balance (blue area), as constrained by the total mass of Cu in the deposit, the estimated Cu concentration, and the resulting volume of magma erupted. The eruption magnitude, *k*, is proportional to the SO_2 yield per eruption (solid line), where it is extrapolated to higher magnitude eruptions (dashed line) (*50*). Both the Hg- and Cu-derived SO_2 emission estimates are consistent with each other and suggest that the eruption was massive and similar in eruption magnitude and SO_2 yield as the Young Toba Tuff and Laki eruptions (red triangles) (*75*, *76*). Notably, it is expected that massive felsic volcanism in South China and rapid global cooling induced by injection of SO_2 in the stratosphere followed by the massive injection of CO_2 into the atmosphere and subsequent atmospheric warming across the EPME from the STLIP event enhanced the severity of the mass extinction event at the PTB. Furthermore, the SO_2 flux estimates from felsic volcanism in South China are considered minimums, since the total mass of Hg and Cu within the EPME interval considered in this study does not take into account the additional mass of Hg and Cu dispersed beyond the deposit in South China. The estimated cooling of the average global annual surface temperatures due to SO_2 emissions into the stratosphere is shown for a range of past large volcanic eruptions (*77*–*79*). Although most of these past large volcanic eruptions have not created conditions that induce mass extinction events, this comparison highlights the potential for much larger swings in temperature over the Paleocene-Eocene Thermal Maximum (PETM) than traditionally envisioned. ka B.P., thousand years before the present.

Therefore, this work strongly suggests that there was rapid cooling, likely >4°C (as a global average; and in the South China Block), followed by an abrupt warming in the end Permian. This temperature trend is consistent with a marked sea level fall at the onset of the EPME followed by an immediate transgression (*15*, *57*). This raises the intriguing possibility that the temperature swings in this time interval were even more pronounced than previously estimated. Rapid cooling on top of longer-term warming increases the climatic extremes experienced by terrestrial ecosystems. This bolsters the case that environmental degradation due to rapid climate shifts was an important kill mechanism during the end-Permian biotic crisis.

For comparison, cooling has been invoked as the kill mechanism for the K-Pg mass extinction, with pronounced biotic effects in areas that do not typically experience freezes [e.g., (*58*, *59*)]. Nonetheless, note that pronounced cooling may have limited biotic effects [e.g., (*60*)] if the temperature change occurred over tens to hundreds of

years as has been predicted with basalt SO_2 injections [e.g., (*61*)]. However, the aerosol fallout times for explosive felsic volcanic events can be rapid [e.g., (*62*)]. In this light, negative biotic effects need not only come from cooling but also from rapid warming. Consistent with this idea, rapid drops in aerosol concentrations can produce warming velocities that surpass even recent and predicted future anthropogenically induced warming—markedly increasing habitat fragmentation and extinction risk (*63*). There will be uncertainties in any attempt to link SO_2 injection rates to an exact extent of cooling and subsequent warming. However, the potential for such a massive release of SO_2—preceding an interval of potentially unprecedented extent of warming—provides an obvious impetus to develop a more robust estimate of the climatic and biotic effects of end-Permian South China explosive volcanism.

The extreme Cu enrichments, Hg concentration spikes, presence of melt inclusions with rich Cu, and sulfides within the EPME interval in South China presented here cannot be explained by late-stage hypothermal fluids, by surface transport with organic materials, nor through distant aerosol transport from STLIP. A massive output of Cu, Hg, and S derived from explosive super-eruptions near the South China Block during the closure of Paleotethys or opening of Neotethys are the most likely explanation for these geochemical patterns and a plausible stressor of the terrestrial EPME, at least, in South China (Fig. 5 and fig. S7). This conclusion does not reject the close temporal correlation between the EPME and STLIP nor the possible involvement of STLIP in the extinction as the data presented here does not allow us to evaluate the relative contribution of the STLIP to the EPME. At present, there is no known causal connection between subduction-related volcanism and the eruption of STLIP. However, the apparent coincidence of these events should be the source of future investigations.

MATERIALS AND METHODS

Materials
We sampled four terrestrial Permian-Triassic boundary sections in South China. They are the GBC, LB, and TSJ sections in Yunnan Province and the LMD section in Sichuan Province. For sample numbers, their detailed stratigraphic positions of all samples, and their results, see the Supplementary Materials, Fig. 2, and table S4.

Major and minor elements analysis
For major and minor elemental analyses, all samples were ground to 200 mesh and digested using a multi-acid digestion (HNO_3—HF—HCl) protocol (*64*). After completing digestion, these solutions were analyzed for the target elements on a quadrupole inductively coupled plasma mass spectrometer (ICP-MS) and ICP optical emission spectrometer at Nanjing Institute of Geology and Palaeontology (NIGP), Chinese Academy of Sciences. Mercury concentrations were determined using a Direct Mercury Analyzer (Lumex RA-915F) at Tianjin University, China.

Organic carbon isotope analysis
For organic carbon isotope ($\delta^{13}C_{org}$) analyses, the sample powder was treated with a mixture of 18% HCl and 40% HF to remove carbonates and silicates. The insoluble residues were rinsed with 18.2-ohm deionized water until neutral, after which the residues were dried in a furnace at 70°C overnight. Analyses of $\delta^{13}C_{org}$ were carried out using a Finnigan MAT-253 MS at NIGP. The analytical

precision is better than ±0.1‰ for $\delta^{13}C_{org}$. The decarbonated sample powder (~20 mg) was capsuled and combusted at 950°C to measure the TOC content using Thermo Fisher Smart NC elemental analyzer at NIGP. The $\delta^{13}C_{org}$ data are reported as per mil relative to Vienna Pee Dee belemnite standard.

Cu isotope analysis
Copper chemical purification was carried out in an overpressured air-filtered cleanroom at the Institute of Surface-Earth System Science (ISESS) of Tianjin University. Fifty milligrams of samples were dissolved in 3 ml HF-HNO_3 (1:1) mixture at 190°C for 48 hours in precleaned Teflon beakers. The resulting solutions were evaporated to dryness on a hot plate at 95°C, and then 1 ml HNO_3 was added to the samples and dried down to remove HF completely. One milliliter of 8.2 M HCl + 0.03% H_2O_2 solution was added to each beaker and maintained at 120°C for 12 hours in an oven. The contents were evaporated to dryness and added 0.25 ml of 8.2 M HCl + 0.03% H_2O_2 to dryness again. This procedure was repeated three times to ensure achieving complete conversion of cations to chloride form.

The protocol of Cu chromatographic separation was adapted from the method by Maréchal *et al.* (*65*). Briefly, Cu was separated from the matrix using anion exchange resin (0.9 ml; 200 to 400 mesh; AG MP-1M, Bio-Rad). After the resin was cleaned with 18.2 megohms of Milli-Q water and 2 M HNO_3, the conditioning of the resin and the loading of the sample (~1000 µg of Cu in 1 ml) were performed using 8.2 M HCl + 0.03% H_2O_2. The matrix elements were eluted with 4 ml of 8.2 M HCl, and Cu was collected in the following 8.2 M HCl (10 ml). The collected Cu fraction was dried, dissolved in 14 M HNO_3 (0.1 ml) and dried again to remove HCl traces. The purified Cu fraction was redissolved in 2% HNO_3 for ICP-MS and multicollector (MC)–ICP-MS measurements. Elemental concentrations were measured on ICP-MS NexION 300X (PerkinElmer, USA), with a precision better than 5% (2 SD). The recovery of the procedure for Cu was assessed by BHVO-2 and JB-2, and the average value of yield was 98 ± 4% (*n* = 8). The total procedural blank was less than 0.1 ng (*n* = 6) for Cu. In most cases, it represented less than 0.1% of Cu from samples and had no notable influence on isotope ratio measurement.

The copper isotopic composition was measured using a Neptune Plus (Thermo Fisher Scientific) at ISESS. Instrumental mass fractionation effects were corrected using a model of standard sample bracketing with internal normalization, and Ga (NIST SRM 3119a) was used as an internal standard, which was added to both sample and standard solution (*65*, *66*). Each measurement consists of a block of 90 cycles of 2 s each, with an outlier exclusion algorithm at 2σ level. All data are presented in delta notation with respect to the NIST SRM 976 international reference material (*65*)

$$\delta^{65}Cu = \left[\frac{R_{sample}^{65/63}}{R_{NIST\ 976}^{65/63}} - 1 \right] \times 1000 \qquad (1)$$

An in-house ERM AE 647 Cu standard was calibrated against the NIST 976 at $\delta^{65}Cu_{ERM\ 647/NIST\ 976} = 0.20 \pm 0.05‰$ (2 SD, *n* = 62) and compared with 0.21 ± 0.05‰, measured by Moeller *et al.* (*67*). $\delta^{65}Cu$ of the basalt standard reference material BHVO-2 was measured at 0.12 ± 0.04‰ (2 SD, *n* = 8), which is in good agreement with recommended value (0.12 ± 0.02‰) (*26*).

Hg isotope analysis

The analysis of Hg isotopic compositions followed the procedures described in Huang et al. (68). Milli-Q water (18.2 megohms) was used for the preparation of all aqueous solutions in an ultraclean room. Borosilicate glass and Teflon bottles, impingers, and sample quartz tubes were acid cleaned, followed by rinsing three times with Milli-Q water, and then baked for 4 hours in a muffle furnace at 460°C. Concentrated HCl (~10 M) and HNO_3 (~15 M) were double distilled and used for preparing all solutions including the acid-trapping solution (2:4:9 ratio of 10 M HCl, 15 M HNO_3, and Milli-Q water). BrCl solution (0.2 M) was made by mixing the concentrated HCl with preheated KBr and $KBrO_3$ powders (>99%, American Chemical Society reagent, Sigma-Aldrich, USA) at 250°C for 12 hours. $SnCl_2$ solution was prepared by dissolving the solid in 1 M HCl and used for online reduction of Hg for isotope (MC-ICP-MS) analysis. A $NH_2OH.HCl$ solution (0.2 g ml^{-1}) was prepared for BrCl neutralization, and the reductants were bubbled for 6 hours, with Hg-free N_2 to remove trace levels of Hg vapor.

The NIST SRM 997 thallium was used for mass bias correction, and the international Hg standard NIST SRM 3133 was used as an isotopic reference (68). During the analysis section, the yellow-red soil GBW07405 (National Center for Standard Materials, Beijing, China) with certified Hg concentrations of 0.29 ± 0.03 ng mg^{-1} was used for method development. The use of soil is technically appropriate, because soils have a complex matrix and are an important component of aquatic sediment.

Hg was extracted and concentrated using the double-combustion and trapping dual-stage protocol (68). The low procedural blank (<0.13 ng, $n = 8$) of the whole dual-stage combustion method was negligible compared to the amount of Hg (>20 ng) in samples. Good recovery (98 ± 4%, 2 SD) guarantees that no Hg isotope fractionation occurred during the preconcentration procedure. Hg isotopes were measured on a Nu MC-ICP-MS at ISESS of Tianjin University. Volatile elemental Hg generated by $SnCl_2$ reduction in the cold vaper generation system was introduced into the plasma through Ar flux. This reduction also served for Hg purification (69). Instrumental mass bias was monitored and corrected using the internal correction and the standard sample bracketing method. The exponential mass fractionation law was applied as the internal correction method assuming the reference $^{205}Tl/^{203}Tl$ value of 2.38714 for the Tl internal standard. The Tl to Hg signal ratio was adjusted to 0.80–1.00.

The result of Hg isotopic measurements was expressed as δ values in units of per mil referenced to the bracketed NIST 3133 Hg standard, as follows

$$\delta^{202}Hg =$$
$$[(^{202}Hg/^{198}Hg)_{sample}/(^{202}Hg/^{198}Hg)_{standard} - 1] \times 1000‰ \quad (2)$$

Any isotope composition that does not follow the theoretical MDF is considered MIF. MIF values are indicated by capital delta (Δ) notation (in per mil) and predicted from $\delta^{202}Hg$ using the following equations

$$\Delta^{199}Hg = \delta^{199}Hg - 0.252 \times \delta^{202}Hg \quad (3)$$

$$\Delta^{201}Hg = \delta^{201}Hg - 0.752 \times \delta^{202}Hg \quad (4)$$

The long-term measurements of GBW07405 yielded mean values of −1.79 ± 0.08‰, −0.30 ± 0.04‰, −0.01 ± 0.02‰, and −0.28 ±

0.03‰ for $\delta^{202}Hg$, $\Delta^{199}Hg$, $\Delta^{200}Hg$, and $\Delta^{201}Hg$ (2 SD, $n = 11$), respectively, in agreement with previous studies (68, 69). Repeated measurements ($n = 15$) of the standard UM-Almaden Hg yielded mean $\delta^{202}Hg$, $\Delta^{199}Hg$, $\Delta^{200}Hg$, and $\Delta^{201}Hg$ values of −0.54 ± 0.11‰, −0.01 ± 0.03‰, 0.00 ± 0.05‰ , and 0.00 ± 0.05 ‰ (2σ), respectively, also in agreement with previous studies (70). The obtained 2σ value is considered typical of uncertainties for samples that were measured only once due to limited mass.

Cu and Hg isotope model constraints

The Cu isotope compositional change was modeled with a Rayleigh fractionation expression to describe open system isotope effects upon increasing degrees of volatilization/degassing from magma upon volcanic eruption (Fig. 4A). The $\delta^{65}Cu$ composition of the magma was assumed to be similar to bulk silicate Earth, 0‰, since the volcanic system likely had undergone notable differentiation, decompression, and oxidization, resulting in the magma becoming undersaturated with respect to sulfide (71). A $\delta^{65}Cu$ fractionation factor up to 0.69‰ between volatized fluid and silicate melt was experimentally determined (72), where the Cu-bearing vapor is enriched in the heavy isotopes relative to the melt. The partition coefficient between exsolved fluid and silicate melt is much greater than one, indicating that Cu will be efficiently removed by exsolved fluid and the $\delta^{65}Cu$ values of the silicate melt will become increasingly negative with continued degassing (72).

Similarly, the Hg isotope compositional change of magma and volatilized fluid was modeled with a Rayleigh fractionation expression to simulate increasing degrees of volatilization/degassing from magma upon eruption (Fig. 4B). The $\delta^{202}Hg$ fractionation factor between volatized fluid and melt is estimated to be −1.00‰, where the vapor is enriched in light isotopes of Hg relative to the degassing magma (73). The $\delta^{202}Hg$ composition of the magma was assumed to be −3‰, which is intermediate in the range expected for the $\delta^{202}Hg$ composition of mantle, approximately between −4.95 and −2.35‰ (73). Furthermore, the initial $\delta^{202}Hg$ value of the degassing magma was chosen to be −3‰ to remain consistent with the entire range of $\delta^{202}Hg$ values observed within the Cu- and Hg-enriched deposits in South China described in this study. Secondary depositional processes of Hg within the volcanic plume, such as the oxidative transformation of Hg^0 to particulate Hg^{2+} (74), are not taken into account in this model, since the deposition of volcanically derived Hsg within the plume into nearby South China was assumed to be nearly quantitative, as supported by the observed elevated Hg/TOC values and their respective odd Hg isotope values, demonstrating limited transport in the atmosphere before deposition.

Together, the Cu and Hg isotope systems suggest a substantial degree of volatilization/degassing from the magma upon volcanic eruption. The highly negative $\delta^{65}Cu$ values, −1.5‰, and large range of increasing $\delta^{202}Hg$ values toward 0‰ suggest that a massive eruption resulted in a notable volatile flux. This is further corroborated by taking into account the total mass of Hg in the deposits compared to the Hg/SO_2 ratio expected for degassing during large explosive eruptions, 10^{-5} to 10^{-4} (51), resulting in a notable flux of degassing SO_2 comparable in magnitude as past super-explosive silicic volcanism events, as demonstrated in Fig. 6.

REFERENCES AND NOTES

1. D. H. Erwin, *Extinction: How Life on Earth Nearly Ended 250 Million Years Ago*. (Princeton Univ. Press, 2006).

2. J. X. Fan, S. Z. Shen, D. H. Erwin, P. M. Sadler, N. MacLeod, Q. M. Cheng, X. D. Hou, J. Yang, X. D. Wang, Y. Wang, H. Zhang, X. Chen, G. X. Li, Y. C. Zhang, Y. K. Shi, D. X. Yuan, Q. Chen, L. N. Zhang, C. Li, Y. Y. Zhao, A high-resolution summary of Cambrian to Early Triassic marine invertebrate biodiversity. *Science* **367**, 272–277 (2020).

3. P. A. Viglietti, R. B. J. Benson, R. M. H. Smith, J. Botha, C. F. Kammerer, Z. Skosan, E. Butler, A. Crean, B. Eloff, S. Kaal, J. Mohoi, W. Molehe, N. Mtalana, S. Mtungata, N. Ntheri, T. Ntsala, J. Nyaphuli, P. October, G. Skinner, M. Strong, H. Stummer, F. P. Wolvaardt, K. D. Angielczyk, Evidence from South Africa for a protracted end-Permian extinction on land. *Proc. Natl. Acad. Sci. U.S.A.* **118**, e2017045118 (2021).

4. S. D. Burgess, S. A. Bowring, High-precision geochronology confirms voluminous magmatism before, during, and after Earth's most severe extinction. *Sci. Adv.* **363**, 862–866 (2015).

5. S. D. Burgess, S. A. Bowring, S. Z. Shen, High-precision timeline for Earth's most severe extinction. *Proc. Natl. Acad. Sci. U.S.A.* **111**, 3316–3321 (2014).

6. M. M. Joachimski, A. S. Alekseev, A. Grigoryan, Y. A. Gatovsky, Siberian Trap volcanism, global warming and the Permian-Triassic mass extinction: New insights from Armenian Permian-Triassic sections. *Geol. Soc. Am. Bull.* **132**, 427–443 (2019).

7. J. Chen, S. Z. Shen, X. H. Li, Y. G. Xu, M. M. Joachimski, S. A. Bowring, D. H. Erwin, D. X. Yuan, B. Chen, H. Zhang, Y. Wang, C. Q. Cao, Q. F. Zheng, L. Mu, High-resolution SIMS oxygen isotope analysis on conodont apatite from South China and implications for the end-Permian mass extinction. *Palaeogeogr. Palaeoclimatol. Palaeoecol.* **448**, 26–38 (2016).

8. Y. Wu, D. Chu, J. Tong, H. Song, J. Dal Corso, P. B. Wignall, H. Song, Y. Du, Y. Cui, Six-fold increase of atmospheric pCO$_2$ during the Permian-Triassic mass extinction. *Nat. Commun.* **12**, 2137 (2021).

9. F. Zhang, S. J. Romaniello, T. J. Algeo, K. V. Lau, M. E. Clapham, S. Richoz, A. D. Herrmann, H. Smith, M. Horacek, A. D. Anbar, Multiple episodes of extensive marine anoxia linked to global warming and continental weathering following the latest Permian mass extinction. *Sci. Adv.* **4**, e1602921 (2018).

10. C. R. Fielding, T. D. Frank, S. McLoughlin, V. Vajda, C. Mays, A. P. Tevyaw, A. Winguth, C. Winguth, R. S. Nicoll, M. Bocking, J. L. Crowley, Age and pattern of the southern high-latitude continental end-Permian extinction constrained by multiproxy analysis. *Nat. Commun.* **10**, 385 (2019).

11. D. Chu, J. Dal Corso, W. Shu, H. Song, P. B. Wignall, S. E. Grasby, B. van de Schootbrugge, K. Zong, Y. Wu, J. Tong, Metal-induced stress in survivor plants following the end-Permian collapse of land ecosystems. *Geology* **49**, 657–661 (2021).

12. S. E. Grasby, X. Liu, R. Yin, R. E. Ernst, Z. Chen, Toxic mercury pulses into late Permian terrestrial and marine environments. *Geology* **48**, 830–833 (2020).

13. S. E. Grasby, T. R. Them II, Z. Chen, R. Yin, O. H. Ardakani, Mercury as a proxy for volcanic emissions in the geologic record. *Earth-Sci. Rev.* **196**, 102880 (2019).

14. J. Shen, J. Chen, T. J. Algeo, S. Yuan, Q. Feng, J. Yu, L. Zhou, B. O'Connell, N. J. Planavsky, Evidence for a prolonged Permian-Triassic extinction interval from global marine mercury records. *Nat. Commun.* **10**, 1563 (2019).

15. S. Z. Shen, J. Ramezani, J. Chen, C. Q. Cao, D. H. Erwin, H. Zhang, L. Xiang, S. D. Schoepfer, C. M. Henderson, Q. F. Zheng, S. A. Bowring, Y. Wang, X. H. Li, X. D. Wang, D. X. Yuan, Y. C. Zhang, L. Mu, J. Wang, Y. S. Wu, A sudden end-Permian mass extinction in South China. *Geol. Soc. Am. Bull.* **131**, 205–223 (2019).

16. V. I. Davydov, E. V. Karasev, The influence of the Permian-Triassic magmatism in the Tunguska Basin, Siberia on the regional floristic biota of the Permian-Triassic transition in the region. *Front. Earth Sci.* **9**, 635179 (2021).

17. Y. Cui, L. R. Kump, Global warming and the end-Permian extinction event: Proxy and modeling perspectives. *Earth-Sci. Rev.* **149**, 5–22 (2015).

18. S. Self, S. Blake, Consequences of explosive supereruptions. *Elements* **4**, 41–46 (2008).

19. B. Zheng, C. Mou, R. Zhou, X. Wang, Z. Xiao, Y. Chen, Nature and origin of the volcanic ash beds near the Permian–Triassic boundary in South China: New data and their geological implications. *Geol. Mag.* **157**, 677–689 (2019).

20. H. Zhang, C. Q. Cao, X. L. Liu, L. Mu, Q. F. Zheng, F. Liu, L. Xiang, L. J. Liu, S. Z. Shen, The terrestrial end-Permian mass extinction in South China. *Palaeogeogr. Palaeoclimatol. Palaeoecol.* **448**, 108–124 (2016).

21. S. Z. Shen, J. L. Crowley, Y. Wang, S. A. Bowring, D. H. Erwin, P. M. Sadler, C. Q. Cao, D. H. Rothman, C. M. Henderson, J. Ramezani, H. Zhang, Y. A. Shen, X. D. Wang, W. Wang, L. Mu, W. Z. Li, Y. G. Tang, X. L. Liu, L. J. Liu, Y. Zeng, Y. F. Jiang, Y. G. Jin, Calibrating the end-Permian mass extinction. *Science* **334**, 1367–1372 (2011).

22. Y. F. Cai, H. Zhang, Z. Feng, S. Z. Shen, Intensive wildfire associated with volcanism promoted the vegetation changeover in Southwest China during the Permian–Triassic transition. *Front. Earth Sci.* **9**, 615841 (2021).

23. Y. Wu, J. Tong, T. J. Algeo, D. Chu, Y. Cui, H. Song, W. Shu, Y. Du, Organic carbon isotopes in terrestrial Permian-Triassic boundary sections of North China: Implications for global carbon cycle perturbations. *Geol. Soc. Am. Bull.* **132**, 1106–1118 (2020).

24. P. D. Ward, J. Botha, R. Buick, M. O. De Kock, D. H. Erwin, G. H. Garrison, J. L. Kirschvink, R. Smith, Abrupt and gradual extinction among Late Permian land vertebrates in the Karoo basin, South Africa. *Science* **307**, 709–714 (2005).

25. R. J. Twitchett, C. V. Looy, R. Morante, H. Visscher, P. B. Wignall, Rapid and synchronous collapse of marine and terrestrial ecosystems during the end-Permian biotic crisis. *Geology* **29**, 351–354 (2001).

26. F. Moynier, D. Vance, T. Fujii, P. Savage, The isotope geochemistry of zinc and copper. *Rev. Mineral. Geochem.* **82**, 543–600 (2017).

27. X. K. Zhu, Y. Guo, R. J. P. Williams, R. K. O'Nions, A. Matthews, N. S. Belshaw, G. W. Canters, E. C. de Waal, U. Weser, B. K. Burgess, B. Salvato, Mass fractionation processes of transition metal isotopes. *Earth Planet. Sci. Lett.* **200**, 47–62 (2002).

28. R. L. Rudnick, S. Gao, in *The Crust: Treatise on Geochemistry*, H. D. Holland, K. K. Turekian, Eds. (Oxford, Elsevier-Pergamon, 2003), pp. 1–64.

29. Y. Zhang, X. Jia, Z. Wang, Provenance of the Late Permian Xuanwei Formation in the upper Yangtze Block: Constraints from the sedimentary record and tectonic implications. *Acta Geol. Sin. Engl.* **93**, 1673–1686 (2019).

30. W. M. Haynes, *CRC Handbook of Chemistry and Physics, 96th Edition (Internet Version 2016)* (CRC Press/Taylor and Francis, 2016).

31. R. Mathur, S. Titley, F. Barra, S. Brantley, M. Wilson, A. Phillips, F. Munizaga, V. Maksaev, J. Vervoort, G. Hart, Exploration potential of Cu isotope fractionation in porphyry copper deposits. *J. Geochem. Explor.* **102**, 1–6 (2009).

32. B. He, Y. T. Zhong, Y. G. Xu, X. H. Li, Triggers of Permo-Triassic boundary mass extinction in South China: The Siberian Traps or Paleo-Tethys ignimbrite flare-up? *Lithos* **204**, 258–267 (2014).

33. X. F. Qin, Z. Q. Wang, Y. L. Zhang, L. Z. Pan, G. A. Hu, F. S. Zhou, Geochronology and geochemistry of Early Mesozoic acid volcanic rocks from southwest Guangxi: Constraints on tectonic evolution of the southwestern segment of Qinzhou-Hangzhou joint belt. *Acta Petrol. Sin.* **27**, 794–808 (2011).

34. C. H. Lo, S. L. Chung, T. Y. Lee, G. Wu, Age of the Emeishan flood magmatism and relations to Permian–Triassic boundary events. *Earth Planet. Sci. Lett.* **198**, 449–458 (2002).

35. L. Li, Z. Yan, Z. Song, S. Tan, X. Li, W. Xin, N. Tian, G. Wang, C. Wang, J. Li, Late Permian-Middle Triassic intermediate-acid intrusive rocks in the Eastern Kunlun Orogenic Belt, NW China: Petrogenesis and implications for geodynamic evolution. *Int. Geol. Rev.* 1–23 (2021).

36. X. Wang, P. A. Cawood, H. Zhao, L. Zhao, S. E. Grasby, Z. Q. Chen, P. B. Wignall, Z. Lv, C. Han, Mercury anomalies across the end Permian mass extinction in South China from shallow and deep water depositional environments. *Earth Planet. Sci. Lett.* **496**, 159–167 (2018).

37. L. Lerchbaumer, A. Audétat, High Cu concentrations in vapor-type fluid inclusions: An artifact? *Geochim. Cosmochim. Acta* **88**, 255–274 (2012).

38. Z. Zajacz, W. Halter, Copper transport by high temperature, sulfur-rich magmatic vapor: Evidence from silicate melt and vapor inclusions in a basaltic andesite from the Villarrica volcano (Chile). *Earth Planet. Sci. Lett.* **282**, 115–121 (2009).

39. M. Hitzman, R. Kirkham, D. Broughton, J. Thorson, D. Selley, in *Economic Geology and the Bulletin of the Society of Economic Geologists One Hundredth Anniversary Volume 1905–2005*, J. W. Hedenquist, J. H. Thompson, R. J. Goldfarb, J. P. Richards, Eds. (2005), vol. 100, pp. 609–642.

40. K. N. Malitch, R. M. Latypov, I. Y. Badanina, S. F. Sluzhenikin, Insights into ore genesis of Ni-Cu-PGE sulfide deposits of the Noril'sk Province (Russia): Evidence from copper and sulfur isotopes. *Lithos* **204**, 172–187 (2014).

41. M. Si, D. S. McLagan, A. Mazot, N. Szponar, B. Bergquist, Y. D. Lei, C. P. J. Mitchell, F. Wania, Measurement of atmospheric mercury over volcanic and fumarolic regions on the North Island of New Zealand using passive air samplers. *ACS Earth Space Chem.* **4**, 2435–2443 (2020).

42. S. N. Lyman, I. Cheng, L. E. Gratz, P. Weiss-Penzias, L. Zhang, An updated review of atmospheric mercury. *Sci. Total Environ.* **707**, 135575 (2020).

43. J. D. Blum, L. S. Sherman, M. W. Johnson, Mercury isotopes in Earth and environmental sciences. *Annu. Rev. Earth Planet. Sci.* **42**, 249–269 (2014).

44. S. Self, M. R. Rampino, The 1963–1964 eruption of Agung volcano (Bali, Indonesia). *Bull. Volcanol.* **74**, 1521–1536 (2012).

45. L. Zhao, C. R. Ward, D. French, I. T. Graham, Mineralogy of the volcanic-influenced Great Northern coal seam in the Sydney Basin, Australia. *Int. J. Coal Geol.* **94**, 94–110 (2012).

46. T. Luppo, M. G. Lopez de Luchi, A. E. Rapalini, C. I. Martinez Dopico, C. M. Fanning, Geochronologic evidence of a large magmatic province in northern Patagonia encompassing the Permian-Triassic boundary. *J. S. Am. Earth Sci.* **82**, 346–355 (2018).

47. R. A. Gastaldo, S. L. Kamo, J. Neveling, J. W. Geissman, C. V. Looy, A. M. Martini, The base of the Lystrosaurus Assemblage Zone, Karoo Basin, predates the end-Permian marine extinction. *Nat. Commun.* **11**, 1428 (2020).

48. D. A. Nelson, J. M. Cottle, Tracking voluminous Permian volcanism of the Choiyoi Province into central Antarctica. *Lithosphere* **11**, 386–398 (2019).

49. P. J. Wallace, Volcanic SO$_2$ emissions and the abundance and distribution of exsolved gas in magma bodies. *J. Volcanol. Geotherm. Res.* **108**, 85–106 (2001).

50. D. M. Pyle, P. D. Beattie, G. J. S. Bluth, Sulphur emissions to the stratosphere from explosive volcanic eruptions. *Bull. Volcanol.* **57**, 663–671 (1996).

51. D. M. Pyle, T. A. Mather, The importance of volcanic emissions for the global atmospheric mercury cycle. *Atmos. Environ.* **37**, 5115–5124 (2003).

52. B. A. Black, R. R. Neely, J.-F. Lamarque, L. T. Elkins-Tanton, J. T. Kiehl, C. A. Shields, M. J. Mills, C. Bardeen, Systemic swings in end-Permian climate from Siberian Traps carbon and sulfur outgassing. *Nat. Geosci.* **11**, 949–954 (2018).

53. S. M. Newby, J. D. Owens, S. D. Schoepfer, T. J. Algeo, Transient ocean oxygenation at end-Permian mass extinction onset shown by thallium isotopes. *Nat. Geosci.* **14**, 678–683 (2021).

54. F. A. Macdonald, R. Wordsworth, Initiation of Snowball Earth with volcanic sulfur aerosol emissions. *Geophys. Res. Lett.* **44**, 1938–1946 (2017).

55. A. Schmidt, S. Leadbetter, N. Theys, E. Carboni, C. S. Witham, J. A. Stevenson, C. E. Birch, T. Thordarson, S. Turnock, S. Barsotti, L. Delaney, W. Feng, R. G. Grainger, M. C. Hort, Á. Höskuldsson, I. Ialongo, E. Ilyinskaya, T. Jóhannsson, P. Kenny, T. A. Mather, N. A. D. Richards, J. Shepherd, Satellite detection, long-range transport, and air quality impacts of volcanic sulfur dioxide from the 2014-2015 flood lava eruption at Bárðarbunga (Iceland). *J. Geophys. Res.-Atmos.* **120**, 9739–9757 (2015).

56. T. J. Aubry, J. Staunton-Sykes, L. R. Marshall, J. Haywood, N. L. Abraham, A. Schmidt, Climate change modulates the stratospheric volcanic sulfate aerosol lifecycle and radiative forcing from tropical eruptions. *Nat. Commun.* **12**, 4708 (2021).

57. S. Z. Shen, C. Q. Cao, C. M. Henderson, X. D. Wang, G. R. Shi, Y. Wang, W. Wang, End-Permian mass extinction pattern in the northern peri-Gondwanan region. *Palaeoworld* **15**, 3–30 (2006).

58. A. A. Chiarenza, A. Farnsworth, P. D. Mannion, D. J. Lunt, P. J. Valdes, J. V. Morgan, P. A. Allison, Asteroid impact, not volcanism, caused the end-Cretaceous dinosaur extinction. *Proc. Natl. Acad. Sci. U.S.A.* **117**, 17084–17093 (2020).

59. J. Vellekoop, A. Sluijs, J. Smit, S. Schouten, J. W. H. Weijers, J. S. Sinninghe Damsté, H. Brinkhuis, Rapid short-term cooling following the Chicxulub impact at the Cretaceous–Paleogene boundary. *Proc. Natl. Acad. Sci. U.S.A.* **111**, 7537–7541 (2014).

60. A. Schmidt, R. A. Skeffington, T. Thordarson, S. Self, P. M. Forster, A. Rap, A. Ridgwell, D. Fowler, M. Wilson, G. W. Mann, P. B. Wignall, K. S. Carslaw, Selective environmental stress from sulphur emitted by continental flood basalt eruptions. *Nat. Geosci.* **9**, 77–82 (2016).

61. M. R. Rampino, S. H. Ambrose, in *Volcanic Hazards and Disasters in Human Antiquity. Geological Society of America Special papers*, F. W. McCoy, G. Heiken, Eds. (Geological Society of America, 2000), vol. 345, pp. 71–82.

62. A. Lambert, R. G. Grainger, J. J. Remedios, C. D. Rodgers, M. Corney, F. W. Taylor, Measurements of the evolution of the Mt. Pinatubo aerosol cloud by ISAMS. *Geophys. Res. Lett.* **20**, 1287–1290 (1993).

63. C. H. Trisos, C. Amatulli, J. Gurevitch, A. Robock, L. Xia, B. Zambri, Potentially dangerous consequences for biodiversity of solar geoengineering implementation and termination. *Nat. Ecol. Evol.* **2**, 475–482 (2018).

64. B. Kendall, C. T. Reinhard, T. W. Lyons, A. J. Kaufman, S. W. Poulton, A. D. Anbar, Pervasive oxygenation along late Archaean ocean margins. *Nat. Geosci.* **3**, 647–652 (2010).

65. C. N. Maréchal, P. Télouk, F. Albarède, Precise analysis of copper and zinc isotopic compositions by plasma-source mass spectrometry. *Chem. Geol.* **156**, 251–273 (1999).

66. Q. Hou, L. Zhou, S. Gao, T. Zhang, L. Feng, L. Yang, Use of Ga for mass bias correction for the accurate determination of copper isotope ratio in the NIST SRM 3114 Cu standard and geological samples by MC-ICPMS. *J. Anal. At. Spectrom.* **31**, 280–287 (2016).

67. K. Moeller, R. Schoenberg, R. B. Pedersen, D. Weiss, S. Dong, Calibration of the new certified reference materials ERM-AE633 and ERM-AE647 for copper and IRMM-3702 for zinc isotope amount ratio determinations. *Geostand. Geoanal. Res.* **36**, 177–199 (2012).

68. Q. Huang, Y. Liu, J. Chen, X. Feng, W. Huang, S. Yuan, H. Cai, X. Fu, An improved dual-stage protocol to pre-concentrate mercury from airborne particles for precise isotopic measurement. *J. Anal. At. Spectrom.* **30**, 957–966 (2015).

69. J. D. Blum, M. W. Johnson, Recent developments in mercury stable isotope analysis. *Rev. Mineral. Geochem.* **82**, 733–757 (2017).

70. S. Yuan, J. Chen, H. Cai, W. Yuan, Z. Wang, Q. Huang, Y. Liu, X. Wu, Sequential samples reveal significant variation of mercury isotope ratios during single rainfall events. *Sci. Total Environ.* **624**, 133–144 (2018).

71. P. S. Savage, F. Moynier, H. Chen, G. Shofner, J. Siebert, J. Badro, I. S. Puchtel, Copper isotope evidence for large-scale sulphide fractionation during Earth's differentiation. *Geochem. Perspect. Lett.* **1**, 53–64 (2015).

72. H. Guo, Y. Xia, R. Bai, X. Zhang, F. Huang, Experiments on Cu-isotope fractionation between chlorine-bearing fluid and silicate magma: Implications for fluid exsolution and porphyry Cu deposits. *Natl. Sci. Rev.* **7**, 1319–1330 (2020).

73. F. Moynier, J. Chen, K. Zhang, H. Cai, Z. Wang, M. G. Jackson, J. M. D. Day, Chondritic mercury isotopic composition of Earth and evidence for evaporative equilibrium degassing during the formation of eucrites. *Earth Planet. Sci. Lett.* **551**, 116544 (2020).

74. T. Zambardi, J. E. Sonke, J. P. Toutain, F. Sortino, H. Shinohara, Mercury emissions and stable isotopic compositions at Vulcano Island (Italy). *Earth Planet. Sci. Lett.* **277**, 236–243 (2009).

75. T. Thordarson, S. Self, Atmospheric and environmental effects of the 1783–1784 Laki eruption: A review and reassessment. *J. Geophys. Res.* **108**, 4011 (2003).

76. C. Oppenheimer, Limited global change due to the largest known Quaternary eruption, Toba ≈74kyr BP? *Quat. Sci. Rev.* **21**, 1593–1609 (2002).

77. S. Sparks, S. Self, D. Pyle, C. Oppenheimer, H. Rymer, J. Grattan, *Super-Eruptions: Global Effects and Future Threats: Report of a Geological Society of London Working Group* (Geological Society of London, ed. 2, 2005), pp.1–24.

78. S. Self, R. Gertisser, T. Thordarson, M. R. Rampino, J. A. Wolff, Magma volume, volatile emissions, and stratospheric aerosols from the 1815 eruption of Tambora. *Geophys. Res. Lett.* **31**, L20608 (2004).

79. D. H. Erwin, T. A. Vogel, Testing for causal relationships between large pyroclastic volcanic eruptions and mass extinctions. *Geophys. Res. Lett.* **19**, 893–896 (1992).

80. M. Ravichandran, Interactions between mercury and dissolved organic matter––A review. *Chemosphere* **55**, 319–331 (2004).

81. J. Shen, J. Yu, J. Chen, T. Algeo, G. Xu, Q. Feng, X. Shi, N. J. Planavsky, W. Shu, S. Xie, Mercury evidence of intense volcanic effects on land during the Permian-Triassic transition. *Geology* **47**, 1117–1121 (2019).

82. R. H. Sillitoe, Supergene oxidized and enriched porphyry copper and related deposits. *Econ. Geol.* **100**, 723–768 (2005).

83. C. Grondahl, Z. Zajacz, Magmatic controls on the genesis of porphyry Cu–Mo–Au deposits: The Bingham Canyon example. *Earth Planet. Sci. Lett.* **480**, 53–65 (2017).

84. C.-T. A. Lee, M. Tang, How to make porphyry copper deposits. *Earth Planet. Sci. Lett.* **529**, 115868 (2020).

85. J. Kim, K. Y. Lee, J. H. Kim, Metal-bearing molten sulfur collected from a submarine volcano: Implications for vapor transport of metals in seafloor hydrothermal systems. *Geology* **39**, 351–354 (2011).

86. C. A. Heinrich, D. Günther, A. Audétat, T. Ulrich, R. Frischknecht, Metal fractionation between magmatic brine and vapor, determined by microanalysis of fluid inclusions. *Geology* **27**, 755–758 (1999).

87. M. Edmonds, T. A. Mather, E. J. Liu, A distinct metal fingerprint in arc volcanic emissions. *Nat. Geosci.* **11**, 790–794 (2018).

88. S. Calabrese, A. Aiuppa, P. Allard, E. Bagnato, S. Bellomo, L. Brusca, W. D'Alessandro, F. Parello, Atmospheric sources and sinks of volcanogenic elements in a basaltic volcano (Etna, Italy). *Geochim. Cosmochim. Acta* **75**, 7401–7425 (2011).

89. R. Mathur, L. Jin, V. Prush, J. Paul, C. Ebersole, A. Fornadel, J. Z. Williams, S. Brantley, Cu isotopes and concentrations during weathering of black shale of the Marcellus Formation, Huntingdon County, Pennsylvania (USA). *Chem. Geol.* **304-305**, 175–184 (2012).

90. S. A. Liu, J. Huang, J. G. Liu, G. Wörner, W. Yang, Y. J. Tang, Y. Chen, L. Tang, J. Zheng, S. Li, Copper isotopic composition of the silicate Earth. *Earth Planet. Sci. Lett.* **427**, 95–103 (2015).

91. W. Li, S. E. Jackson, N. J. Pearson, O. Alard, B. W. Chappell, The Cu isotopic signature of granites from the Lachlan Fold Belt, SE Australia. *Chem. Geol.* **258**, 38–49 (2009).

92. R. Mathur, J. Ruiz, M. J. Casselman, P. Megaw, R. van Egmond, Use of Cu isotopes to distinguish primary and secondary Cu mineralization in the Cañariaco Norte porphyry copper deposit, Northern Peru. *Mineral. Deposita* **47**, 755–762 (2012).

93. W. Li, S. E. Jackson, N. J. Pearson, S. Graham, Copper isotopic zonation in the Northparkes porphyry Cu–Au deposit, SE Australia. *Geochim. Cosmochim. Acta* **74**, 4078–4096 (2010).

94. G. Markl, Y. Lahaye, G. Schwinn, Copper isotopes as monitors of redox processes in hydrothermal mineralization. *Geochim. Cosmochim. Acta* **70**, 4215–4228 (2006).

95. S. Ehrlich, I. Butler, L. Halicz, D. Rickard, A. Oldroyd, A. Matthews, Experimental study of the copper isotope fractionation between aqueous Cu(II) and covellite, CuS. *Chem. Geol.* **209**, 259–269 (2004).

96. A. Fernandez, D. M. Borrok, Fractionation of Cu, Fe, and Zn isotopes during the oxidative weathering of sulfide-rich rocks. *Chem. Geol.* **264**, 1–12 (2009).

97. D. Asael, A. Matthews, M. Bar-Matthews, Y. Harlavan, I. Segal, Tracking redox controls and sources of sedimentary mineralization using copper and lead isotopes. *Chem. Geol.* **310-311**, 23–35 (2012).

98. T. Fujii, F. Moynier, M. Abe, K. Nemoto, F. Albarède, Copper isotope fractionation between aqueous compounds relevant to low temperature geochemistry and biology. *Geochim. Cosmochim. Acta* **110**, 29–44 (2013).

99. T. F. D. Mason, D. J. Weiss, J. B. Chapman, J. J. Wilkinson, S. G. Tessalina, B. Spiro, M. S. A. Horstwood, J. Spratt, B. J. Coles, Zn and Cu isotopic variability in the Alexandrinka volcanic-hosted massive sulphide (VHMS) ore deposit, Urals, Russia. *Chem. Geol.* **221**, 170–187 (2005).

100. P. B. Larson, K. Maher, F. C. Ramos, Z. Chang, M. Gaspar, L. D. Meinert, Copper isotope ratios in magmatic and hydrothermal ore-forming environments. *Chem. Geol.* **201**, 337–350 (2003).

101. M. Haest, P. Muchez, J. C. Petit, F. Vanhaecke, Cu isotope ratio variations in the Dikulushi Cu-Ag deposite, DRC: Of primary origin or induced by supergene reworking. *Econ. Geol.* **104**, 1055–1064 (2009).

102. Z. Feng, H. B. Wei, Y. Guo, X. Y. He, Q. Sui, Y. Zhou, H. Y. Liu, X. D. Gou, Y. Lv, From rainforest to herbland: New insights into land plant responses to the end-Permian mass extinction. *Earth-Sci. Rev.* **204**, 103153 (2020).

103. S. E. Grasby, W. J. Shen, R. S. Yin, J. D. Gleason, J. D. Blum, R. F. Lepak, J. P. Hurley, B. Beauchamp, Isotopic signatures of mercury contamination in latest Permian oceans. *Geology* **45**, 55–58 (2017).

104. J. Chen, H. Hintelmann, X. Feng, B. Dimock, Unusual fractionation of both odd and even mercury isotopes in precipitation from Peterborough, ON, Canada. *Geochim. Cosmochim. Acta* **90**, 33–46 (2012).

105. W. Zheng, D. Obrist, D. Weis, B. A. Bergquist, Mercury isotope compositions across North American forests. *Global Biogeochem. Cy.* **30**, 1475–1492 (2016).

106. C. R. Scotese, Atlas of Middle & Late Permian and Triassic Paleogeographic Maps, maps 43–48 from Volume 3 of the PALEOMAP Atlas for ArcGIS (Jurassic and Triassic) and maps 49–52 from Volume 4 of the PALEOMAP PaleoAtlas for ArcGIS (Late Paleozoic) (Mollweide Projection, PALEOMAP Project, map 49, 2014).